Article

Rate dependent performance related to crystal structure evolution of Na0.67Mn0.8Mg0.2O2 in a sodium-ion battery

Neeraj Sharma, Nuria Tapia-Ruiz, Gurpreet Singh, A. Robert Armstrong, James C. Pramudita, Helen E.A. Brand, Juliette Billaud, Peter G. Bruce, and Teofilo Rojo

Just Accepted

Rate dependent performance related to crystal structure evolution of $Na_{0.67}Mn_{0.8}Mg_{0.2}O_2$ in a sodium-ion battery.

Neeraj Sharma[1,*], Nuria Tapia-Ruiz[2], Gurpreet Singh[3], A. Robert Armstrong[4], James C. Pramudita[1], Helen E. A. Brand[5], Juliette Billaud[4], Peter G. Bruce[2], Teofilo Rojo[3,6,*]

[1]School of Chemistry, UNSW Australia, Sydney NSW 2052, Australia

[2]Department of Materials, University of Oxford, Oxford OX1 3PH, UK

[3]CICenergigune, Parque Tecnológico de Álava, Albert Einstein 48, ED.CIC, 01510, Miñano, Spain

[4]School of Chemistry, University of St. Andrews, St. Andrews, Fife KY16 9ST, UK

[5]Australian Synchrotron, 800 Blackburn Road, Clayton 3168, Australia

[6]Departamento de Química Inorgánica, Universidad del País Vasco UPV/EHU, P.O. Box. 644, 48080, Bilbao, Spain

KEYWORDS Cathode, in-situ synchrotron X-ray diffraction, sodium evolution, in-operando

ABSTRACT: Sodium-ion batteries are considered as a favourable alternative to the widely-used lithium-ion batteries for applications such as grid-scale energy storage. However, to meet the energy density and reliability that is necessary, electrodes that are structurally stable and well characterised during electrochemical cycling need to be developed. Here we report on how the applied discharge current rate influences the structural evolution of $Na_{0.67}Mn_{0.8}Mg_{0.2}O_2$ electrode materials. A combination of *ex situ* and *in situ* X-ray diffraction (XRD) data were used to probe the structural transitions at the discharged state and during charge/discharge. *Ex situ* data shows a two-phase electrode at the discharged state comprised of phases that adopt *Cmcm* and *P6₃/mmc* symmetries at the 100 mA/g rate but a predominantly *P6₃/mmc* electrode at 200 and 400 mA/g rates. *In situ* synchrotron XRD data at 100 mA/g shows a solely *P6₃/mmc* electrode when 12 mA/g charge and 100 mA/g discharge is used even though *ex situ* XRD data shows the presence of both *Cmcm* and *P6₃/mmc* phases. The *in situ* data allows the Na site occupancy evolution to be determined as well as the rate of lattice expansion and contraction. Electrochemically, lower applied discharge currents, e.g. 100 mA/g produce better capacity than higher applied currents, e.g. 400 mA/g, and this is related in part to the quantity of the *Cmcm* phase that is formed near the discharged state during a two-phase reaction (*via ex situ* measurements), with lower rates producing more of this *Cmcm* phase. Thus producing more *Cmcm* phase allows access to higher capacities while higher rates show a lower utilisation of the cathode during discharge as less (if any) *Cmcm* phase is formed. Therefore, this work shows how structural transitions can depend on the electrochemically applied current which has significant ramifications on how sodium-ion batteries, and batteries in general, are analysed for performance during operation.

Introduction

Sodium-ion batteries (NIBs) are currently being re-investigated following their inception in 1980's[1] due to the increasing energy demand and the requirement to find alternatives to Li-ion storage. This requirement is further motivated by the elevated price of Li as well as the relatively limited and politically controlled character of Li-sources[2,3]. Sodium-ion batteries have the potential to be perfect candidates for the next generation of batteries due to their high abundance (6th most abundant element in Earth) and wide distribution, giving them excellent economic viability. Notably, Na-ion batteries may find important use in large-scale grid systems (where energy density is a less prominent factor) which store energy from renewable and intermittent sources such as solar and wind.

Currently, cathode materials for NIBs are the most actively researched. Structures that form layered oxides, of the type Na_yMO_2 (where M is a first-row transition metal or a combination of transition metals), are shown to be promising cathode materials for Na-ion batteries due to their high reversible capacity, and for M = Fe and Mn, cost and safety[2-4]. These materials share many common features with their Li-counterparts despite the larger size of Na. Sodium layered oxides are typically identified using Delmas' notation[5] P2, P3, O3, etc., where P, O indicates the Na sites (P = trigonal prismatic and O = octahedral) and the number relates to the transition metal layers within the unit cell. From this classification, numerous studies have been reported for P2-type Na_yMO_2 materials demonstrating their higher capacities, diffusion rate and better cyclability than that of the O3 structure[6].

In 1999, Paulsen and Dahn reported an exhaustive study on P2-sodium manganese oxide compounds[7] after reports from Parant *et al.*, two decades prior, first showed evidence of this phase while elucidating the phase diagram of Na_xMnO_2[8]. Even then, these authors anticipated that Li and transition metal doping in P2-$Na_yMn_xM_zO_2$ reduces the Mn^{3+} Jahn-Teller distortion which in turn, increases its temperature stability range. Billaud *et al.* more recently reported the P2-type $Na_{0.67}Mn_{1-x}Mg_xO_2$ material, where $0 \leq x \leq 0.2$, exhibits a capacity of 175 mA h/g with excellent capacity retention. They

attributed the high cycle efficiency to the Mg dopant, albeit with the tradeoff of less capacity (150 mA h/g for $Na_{0.67}Mn_{0.8}Mg_{0.2}O_2$)[9]. Furthermore, Mg prevented Mn^{3+}/Mn^{4+} ordering within the structure during charge/discharge which was reflected in a reduction of the sharp drops of voltage in the electrochemical curves. Shortly after, Yabuuchi et al. reported on the performance of P2-type $Na_{2/3}Mg_{0.28}Mn_{0.72}O_2$, showing capacities (> 200 mA h/g)[10] higher than those expected for the Mn^{3+}/Mn^{4+} redox couple. A possible explanation given for these results was a reversible oxygen redox reaction, analogous to O3-type lithium-excess manganese oxides[11]. This material, however, showed poor cyclability with a drop in capacity to 150 mA h/g after just 30 cycles.

To our knowledge there are few reports in the literature showing enhanced fast-rate performance in sodium layered cathode materials. Kim et al. reported superior rate capability for $Na_{0.85}Li_{0.17}Ni_{0.21}Mn_{0.64}O_2$ (a capacity of 65 mA h g^{-1} at a rate of 25 C)[12]. More recently, Komaba et al. reported a large reversible capacity (> 100 mA h/g) for $NaFe_{1/2}Co_{1/2}O_2$ after 50 cycles for a 30 C rate (7.23 A/g) in the voltage range, 2.5-4 V[13].

Here we report variable-rate discharge cycling studies on P2-$Na_{0.67}Mn_{0.8}Mg_{0.2}O_2$ electrodes. Galvanostatic measurements coupled with *in situ* and *ex situ* XRD data have been used to demonstrate the effects of the current in the electrochemical performance of this material which in turn, is intrinsically related to the structural phases observed during cycling.

Experimental

Electrochemical performance of $Na_{0.67}Mn_{0.8}Mg_{0.2}O_2$ has been evaluated using CR2032 coin cells. Electrode active materials were mixed with carbon black as conductive agent and polyvinylidene fluoride (PVDF) as binder in a 80:10:10 ratio. The slurry of the composite was made by using N-methylpyrrolidone (NMP) and then the mixture was coated on aluminum foil which acts as current collector. Coated aluminum foils were dried at 120 ^{o}C for two hours in a vacuum oven. Electrodes of 12 mm diameter were punched out of the coated foil and pressed under a load of 4 tons. After pressing the electrodes these were again dried in a vacuum oven at 120 ^{o}C for two hours. 1M $NaPF_6$ in ethylene carbonate and propyl carbonate (EC:PC, 1:1 vol%) was used as electrolyte and sodium metal was used as reference electrode. Galvanostatic cycling was performed in the voltage region of 1.5 – 4 V on a Maccor battery tester. Charging of all samples was performed at 12 mA/g and discharging was performed at different rates *viz.* 100, 200 and 400 mA/g. Initially variable electrode loading was used (e.g., 1.1, 3.2 and 1.1 mg for 100, 200 and 400 mA/g discharge rates respectively, see supporting information Figures S1 and S2); however, for better comparison between applied current rates, electrode loadings were kept consistent at 4.3 ± 0.5 mg. Extended galvanostatic cycling for 100 charge/discharge cycles was undertaken with the above discharge rates and cells were opened in the discharged state (i.e., ~ 1.5 V) at the end of 100 cycles. Electrode loading for these cells at the 100 and 400 mA/g discharge rate were 1.1 mg and 3.2 mg for the 200 mA/g discharge rate. Coated Al foils were washed with electrolyte solvent and dried inside the glove box. Al foils with electrode were mounted on the sample holder and covered with the Kapton foil before collecting XRD data. XRD data were collected using Cu Kα radiation on a Bruker D8 Advance X-ray diffractometer equipped with a LYNXEYE detector. The discharged state of electrodes extracted from *in situ* cells (see below) at the charge rate of 12 mA/g and discharge rates of 100 and 200 mA/g were collected using a PANalytical Empyrean diffractometer with Cu Kα radiation. Electrodes were mounted in an air-tight dome sample holder inside the glovebox and transferred to the instrument. 2 x ≤ 0.5 (vertical) and 4 x ≤ 0.5 (vertical) mm incoming X-ray slits were used for this experiment and further details are presented in the discussion section of this work.

An alternative method to prepare samples for *ex situ* diffraction measurements on the first charge/discharge were used to increase the quantity of the active material in the X-ray beam and thus improve XRD signal. Pellets of active material, super S carbon and Kynar Flex 2801 (a co-polymer based on PVDF) binder in a mass ratio of 75:18:7 were used and after cycling, the electrodes were washed and dried in a similar manner to the coated electrodes. The extracted powders were then transferred to 0.5 mm glass capillaries. *Ex situ* powder XRD measurements for the first cycle were performed on a Stoe STADI/P diffractometer operating in capillary mode, with FeKα_1 radiation (λ = 1.936 Å) and data were collected overnight. Rietveld refinements of the structural models and XRD data were carried out using the program Topas Academic[14].

The positive electrodes for *in situ* measurements were manufactured by mixing 80 % wt. $Na_{0.67}Mn_{0.8}Mg_{0.2}O_2$ active material, 10 % wt. conductive carbon (Super C65) and 10 % wt. PVDF. A few mL of NMP were added and the resulting slurry was stirred for 1 h. This slurry was then coated on an aluminium foil using similar techniques to that described above. Coin cells with 3 mm diameter holes in the casing and 5 mm diameter holes in the stainless spacer were used for the construction of the coin cells for the *in situ* measurements. The coin cells contained Na metal (~1 mm thickness), glass fibre separator with 1M $NaClO_4$ in EC:PC (1:1 wt%) electrolyte solution. *In situ* synchrotron X-ray diffraction experiments were performed within 1-2 days after cell construction. Further details regarding coin cell construction and beamline setup can be found in[15-20].

For the electrochemical tests in coin cells the electrode loading were kept consistent at 4.3 ± 0.5 mg for the discharging rates of 100, 200 and 400 mAh/g. It is worthwhile to note that $NaClO_4$ electrolyte can be dangerous as it is sensitive to shocks and for the development of commercial batteries an alternative electrolyte is preferable. Note following the drying step under vacuum the samples were minimally exposed to air (< 1 minute) if at all. If transportation of samples or electrodes were required they were transported in inert conditions and further dried under vacuum prior to cell construction. This was to avoid CO_2 and moisture uptake into these samples as recently evidenced[21].

In situ synchrotron XRD data were collected on the Powder Diffraction beamline[22] at the Australian Synchrotron with a λ of 0.68954(2) Å, determined using the NIST 660b LaB$_6$ standard reference material. Data were collected continuously in 4.4 minute acquisitions on the coin cell in transmission geometry throughout the charge/discharge cycles. The coin cells were first charged to 4 V at 12 mA/g, then discharged to 1.5 V at 100 mA/g, and charged again to 4 V at 12 mA/g. This corresponds to 0.1-0.2 C on charge and ~1 C on discharge and the electrode loading was 3 mg. Rietveld refinements were carried out using the GSAS[23] software suite with the EXPGUI[24] software interface.

Results and discussion

Electrochemical performance of Na$_{0.67}$Mg$_{0.2}$Mn$_{0.8}$O$_2$ at different rates of discharge

Galvanostatic charge/discharge curves of the samples at various discharge rates are shown in Figure 1. During first charge, which corresponds to the extraction of sodium from Na$_{0.67}$Mg$_{0.2}$Mn$_{0.8}$O$_2$, the Mn^{3+}/Mn^{4+} oxidation process leads to a charging capacity of ~35 mAh/g. During first discharge, which corresponds to sodium insertion into Na$_x$Mg$_{0.2}$Mn$_{0.8}$O$_2$, due to the presence of the sodium metal as the source of the sodium ions a greater amount of sodium ions are inserted into the structure compared to the amount extracted during first charge. This leads to high discharge/charge capacities on the second cycle and subsequent cycling. Interestingly, independent of the discharge rate a large voltage plateau was observed below 2.0 V that contributes significantly to the total capacity.

(a)

(b)

(c)
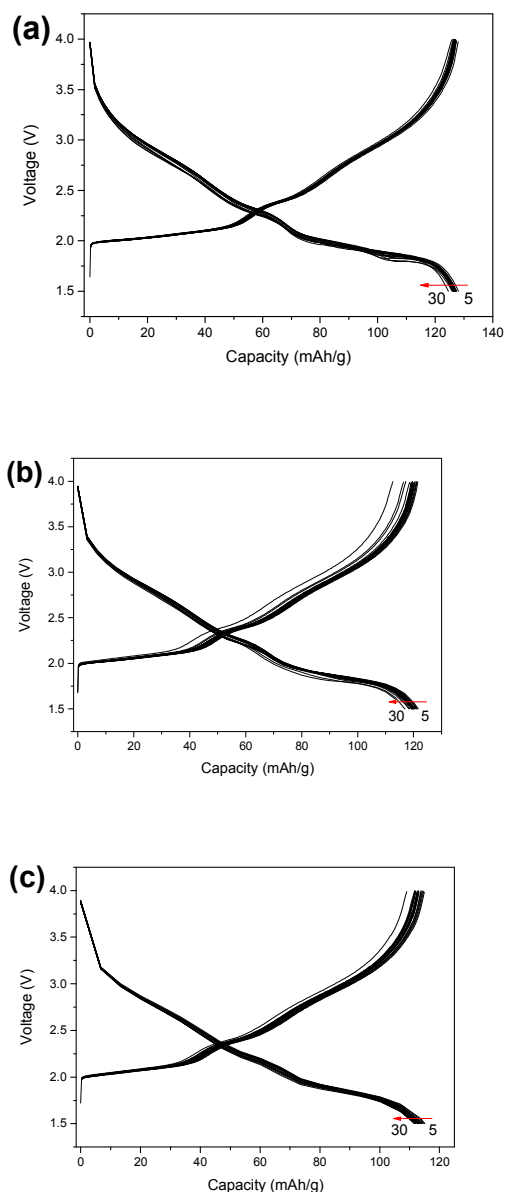
Figure 1. The potential profiles of the Na$_{0.67}$Mn$_{0.8}$Mg$_{0.2}$O$_2$ electrode charged at 12 mA/g and discharged at (a) 100, (b) 200 and (c) 400 mA/g. Profiles from the 5th to 30th cycles are shown.

Cycling performance of the material at different rates of discharge is shown in Figure 2 with two different electrode loadings. Samples were discharged at 100 (low), 200 (moderate) and 400 mA/g (high) rates. Comparing the rates of discharge, the measured capacity from the highest to lowest follows 100 mA/g > 200 mA/g > 400 mA/g using both electrode loads. After 30 cycles at the 4.3 ± 0.5 mg electrode loading the capacity using discharge rates of 100 mA/g, 200 mA/g and 400 mA/g was 125 mAh/g, 120 mAh/g and 114 mAh/g respectively. The observed capacities at these discharge rates are similar which suggest changes when increasing applied discharge rate.

The data presented here are from reproducible cells with very similar electrode loading. We note, however, that there is variation during cell construction (e.g. calandering of the foils and loading density) which does impact electrochemical performance and cannot be completely neglected. It is interesting to note that one series of cells appeared to show optimal performance at the 200 mA/g discharge rate; however, on further analysis this appeared to be a result of the electrode loading (see supporting information, Figures S1-2). In any case, in order to understand the mechanisms responsible for the current-rate dependent behavior we have analyzed the samples by *ex situ* X-ray diffraction (XRD) after 1 and 100 cycles in the fully discharged state at different rates and *in situ* XRD with 12 mA/g charge and 100 mA/g discharge. The *ex situ* data essentially represent extracted data after charge/discharge cycling while the *in situ* data represent the optimal conditions found from the electrochemical results, Figures 1 and 2.
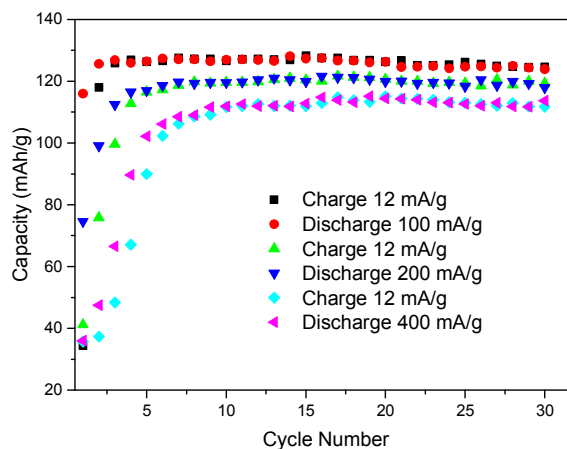
Figure 2. The capacity retention at 12 mA/g charge and 100, 200, 400 mA/g discharge rates for electrode loading of 4.3 ± 0.5 mg.

***Ex situ* structural analysis**

XRD data were obtained from samples extracted at various points on the first charge-discharge cycle at a rate of 10 mA/g. Rietveld refinement of structural models with the data from all points on the first charge revealed that the hexagonal P2 structure (space group *P6$_3$/mmc*) was maintained to full charge, with no formation of the OP4 phase which is observed for lower Mg contents[9]. A smooth contraction in Mn(Mg)-O bond

lengths was observed on sodium extraction accompanying a contraction in *a* and expansion in *c* lattice parameters. The plateau around 2 V on discharge is associated with a transition to an orthorhombic phase (space group *Cmcm*). A profile fit is shown in Figure 3 and refined parameters are given in Table 1. It should be noted that the magnitude of the orthorhombic distortion at the end of discharge is significantly smaller than that observed for lower Mg contents[9]. In addition the Mn(Mg)-O bond lengths show a smaller Jahn-Teller distortion with apical bond lengths of 2.102(11) Å and in-plane distances of 1.938(8) Å, compared to 2.345(3) Å and 1.936(2) Å for 5% Mg.

Table 1. Refined crystallographic parameters for $Na_{0.92}Mn_{0.8}Mg_{0.2}O_2$, space group *Cmcm*. a = 2.8944(6) Å, b = 5.3928(10) Å, c = 10.801(3) Å, R_{wp} = 4.80 %, R_e = 4.54 %, R_p = 3.69 %.

Atom	Wyckoff symbol	x/a	y/b	z/c	SOF	B_{iso}
Na1	4c	0	0.310(2)	0.25	0.86(1)	1.2(-)
Na2	4c	0	0	0.25	0.055(8)	1.2(-)
Mn1/ Mg1	4a	0	0	0	0.8/0.2	0.5(-)
O1	8f	0	0.655(2)	0.0907 (10)	1	0.6(-)
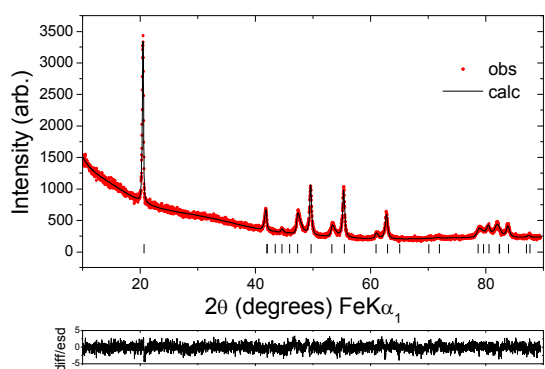
Figure 3. Fitted powder XRD pattern for $Na_{0.92(1)}Mn_{0.8}Mg_{0.2}O_2$ at the end of 1st discharge. Dots represent the observed data and the solid line the calculated pattern. The lower line is the difference/esd. Tick marks indicate the allowed reflections.

The key aspect the first cycle illustrated was the formation of the orthorhombic *Cmcm* phase at 2 V (Table 1 and Figure 3). To observe the discharged products in more detail, cells were cycled 100 times and extracted at the end of discharge. Initial comparison of the 002 type reflections as a function of discharge rate shows obvious split reflections in the case of the sample discharged at 100 mA/g while higher rates of discharge, 200 and 400 mA/g do not show obvious splitting (Figure 4a). Rietveld analysis was used to model the phases and the fit to the data obtained from the sample discharged at 100 mA/g is shown in Figure 4b with further structural details presented in Table 2. The amount of the *Cmcm* phase that forms at the end of discharge decreases as the current rate is increased, with the cell discharged at 400 mA/g showing a wholly *P6₃/mmc* electrode. Therefore, there appears to be a current dependent formation of the *Cmcm* phase at the end of discharge with slower current rates favouring the formation of this phase, while higher current rates show a predominant *P6₃/mmc* phase.

In addition to the phase fractions and lattice parameters presented in Table 2, refinements were performed to approximate the sodium content in the respective phases. Na content was found to increase from 0.68 to 0.75 in the *P6₃/mmc* phase obtained after discharging at 400 mA/g to discharging at 200 mA/g. This corresponds to the greater capacity observed during cycling for discharge at 200 mA/g compared to 400 mA/g.

Correlating the current-dependent formation of the *Cmcm* phase (Figure 4) to the observed current-dependent electrochemical behaviour (Figure 1), it appears that the formation of a significant amount of the *Cmcm* phase at the end of discharge at 100 mA/g is desirable for the performance of these electrodes. Electrochemically there is insufficient charge transfer at the 200 and 400 mA/g rates to capture or extract the entire charge/discharge capacity of the battery. At the discharge rates of 100 and 200 mA/g there exists a mix of *Cmcm* and *P6₃/mmc* phases, but the electrode would have sufficient time to relax or phase separate during extraction and subsequent XRD data analysis, therefore *in situ* XRD was used to study the real-time behaviour of the electrode to determine the precise structural evolution of the electrode at the 100 mA/g discharge rate.

Table 2. Comparative parameters from the structural analysis of extracted electrodes from the discharged state using different current rates.

Extracted from	Phase fraction *Cmcm*: *P6₃/mmc*	Lattice parameters *Cmcm*			Lattice parameters *P6₃/mmc*	
		a	b	C	a	c
12 / 100 mA/g	3.7(3):1	2.9081(4)	5.1848(9)	11.0354(7)	2.8726(9)	11.135(2)
12 / 200 mA/g	0.34(2):1	2.9080(5)	5.2336(7)	11.078(1)	2.9136(5)	11.1370(8)
12 / 400 mA/g	0.002(2):1				2.9177(3)	11.1690(4)
	All *P6₃/mmc*					

Figure 4. (a) The evolution of the 002 type reflection of extracted electrodes at different discharge rates after 100 cycles of charge/discharge. The two phase behaviour is clearly evident during the 100 mA/g discharge while it is predominantly single phase for higher discharging rates. (b) Rietveld refined fit of the $P6_3/mmc$ and $Cmcm$ models and Al to the ex *situ* XRD dataset of the 100 mA/g discharged sample. Data are shown as crosses, the calculated Rietveld model as a line through the data, and the difference between the data and the model as the line below the data. The vertical reflection markers are for the phases labelled. The inset in (b) shows the fit to the two structural models.

In situ synchrotron XRD structural analysis at 200 mA/g discharge

Initial structural characterization:

The cathode in the coin cell adopts a layered structure in the hexagonal space group $P6_3/mmc$ symmetry, a P2-type structure[25] and the reported structural model[8,10] was used as a starting point for analysis. No evidence of CO_2 or water uptake[21] was found with the collected data. Other models, e.g. O3, were trialed but the P2-type structure gave the best fit. Reflections arising from the aluminium current collector and sodium anode were excluded as their positions did not overlap

with many cathode reflections. The background, scale and lattice parameters were refined initially and the Mg/Mn site was modelled with 0.2/0.8 occupation. Two Na sites were present Na(1) with $x = y = 0$ and $z = 1/4$ and Na(2) with $x = 1/3$, $y = 2/3$ and $z = 3/4$ and Na(1) shows lower occupancy than the Na(2) site. Atomic parameters were refined, starting with independently refined atomic displacement parameters (ADPs), oxygen z positional parameter and sodium site occupancy factors (SOFs). Note, sodium ADPs and SOFs were not simultaneously refined, SOFs were refined and fixed, and then the ADPs refined and fixed and so on. In conjunction, profile terms were refined. The structural model fitted well with the data but showed a large mis-match in the 100, 110 and 103 reflections. Fourier maps were used to illustrate what could cause these mis-matches. The difference Fourier map (observed – calculated) is shown in Figures 5a and 5b, in this case the Na sites were set to 0 and the positive Fourier density is shown. There appears to be Fourier density around the Mn/Mg site and at the Na(1) and Na(2) sites, further confirming the P2 structure. Interestingly the Fourier density on the Na(2) site has a distinct non-spherical shape suggesting that this site should be modelled using anisotropic ADPs or reflecting the disordered nature of this site[26]. The inclusion of a preferred orientation term along the 100 axis (0.719(4)) improves the fit, see Figures 5c and 5d, lowers the Na content on both sites to unrealistic values (Na(1) = 0.162(5) and Na(2) = 0.216(8)) and pushes the oxygen positional parameter to a very low value of $z = 0.0704(5)$ but has little influence on the other parameters. The final refined lattice and atomic parameters based on the fits without the preferred orientation term (Figure 5c) is shown in Table 3.

Table 3. Refined crystallographic parameters for $Na_{0.64(1)}Mn_{0.8}Mg_{0.2}O_2$.

Atom	Wyckoff	x	y	Z	SOF	Isotropic ADP ($\times 100$)/Å^2
Na(1)	2	0	0	0.25	0.240(6)	1.08*
Na(2)	2	1/3	2/3	0.75	0.40(1)	6.00*,^
Mn(1)	2	0	0	0	0.8	0.34*,#
Mg(1)	2	0	0	0	0.2	0.34*,#
O(1)	4	1/3	2/3	0.0803(5)	1	1.40*

*Refined alternatively to SOFs and refined and fixed. ^ can be modelled anisotropically as 2.01, 1.00, 0.0, 2.01, 0.0, 13.9. # Constrained to be equal. Spacegroup = $P6_3/mmc$, in Figure 5c, without preferred orientation 34 refinement parameters, $\chi^2 = 1.63$, $R_p = 2.57$ %, wRp = 3.78 %, $a = 2.8717(1)$, $c = 11.1811(2)$ Å.
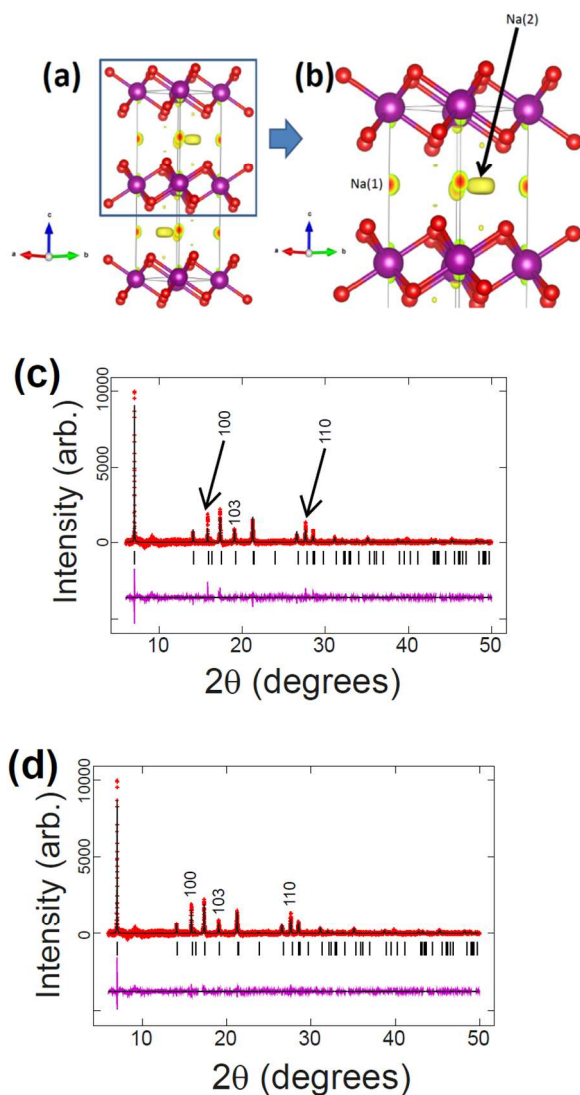
Figure 5. (a, b) The crystal structure of the cathode at OCP with Fourier intensity illustrated when the Na occupancy is set to zero. Mn/Mg is purple, oxygen is red, Fourier intensity as yellow and the sites are labelled. Rietveld refined fit of the structural model to the initial *in situ* synchrotron XRD dataset (c) without and (d) with a preferred orientation term. Data are shown as crosses, the calculated Rietveld model as a line through the data, and the difference between the data and the model as the line below the data. The vertical reflection markers are for P2-$Na_{0.67}Mn_{0.8}Mg_{0.2}O_2$ and the arrows indicate in (c) the 100 and 110 reflections.

Phase evolution:

The phase evolution during charge/discharge/charge is predominantly solid solution with a small two-phase region or plateau (orange shading) as shown in Figure 6 for the 002 and 110 reflections. On visual inspection the electrode does not phase separate (e.g. both $P6_3/mmc$ and *Cmcm* orthorhombic phases existing or transforming between each other) on discharge. During the solid solution regions, the changes in the 2θ-value of the 002 reflection are opposite to the changes in 110 reflection, e.g., as the 002 2θ-value increases the 110 2θ-value decreases. This suggests an anisotropic evolution of the lattice parameters within this Na composition.
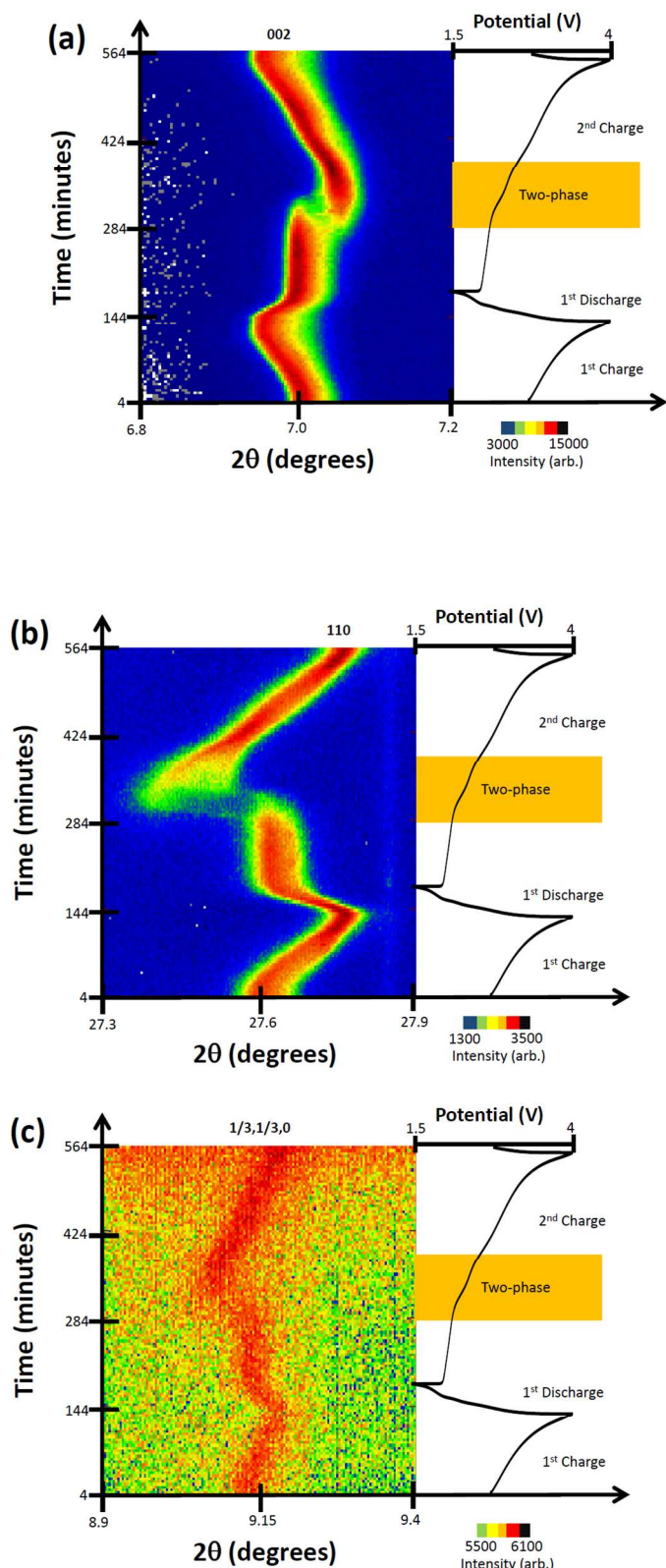
Figure 6. Selected 2θ regions of *in situ* synchrotron XRD data highlighting the evolution of the (a) 002, (b) 110 and (c) 1/3,1/3,0 (Mn/Mg ordering[10]) reflections by a colour scale and the potential profile (right). The orange shaded box highlights the two-phase region showing the disappearance and appearance of reflections.

It is interesting to note that the Mg/Mn ordering observed by Yabuuchi et al.[10] is observed in these data by the 1/3,1/3,0 reflection. This ordering is persistent throughout the charge/discharge cycles (Figure 6c) suggesting that the Mg/Mn ordering does not change during cycling. Additionally, this ordering is observed in the 1st and 2nd phase (discussed below). Note this reflection sits directly above the amorphous feature due to carbon black and PVDF in the electrode mix which reduces its signal-to-noise ratio.

Taking a closer look at the two-phase region, using stacked plots (Figure 7), the relative similarity of the two-phases becomes more apparent. The two-phases adopt the same symmetry and feature only subtle differences in the atomic parameters, predominantly sodium content similar to findings for $LiCoO_2$[27,28] and $Na_{3-y}V_2O_2(PO_4)_2F$[18,19] where two-phase regions are characterized by Na/Li-rich and Na/Li-poor phases. Note the 1st phase disappears with minimal change in 2θ-value (or lattice parameters, see red arrow in Figure 7) while the 2nd phase appears and shows a small change in 2θ-value (see purple arrow in Figure 7) during the two-phase region. The change in 2θ-value is minute but suggests a simultaneous presence of multiple phase transitions, two-phase and solid solution, similar to that observed recently by *in situ* neutron powder diffraction experiments with $LiFePO_4$ cathodes[29]. Note the simultaneous phase transition region is very small in this cathode.

(a)

(b)
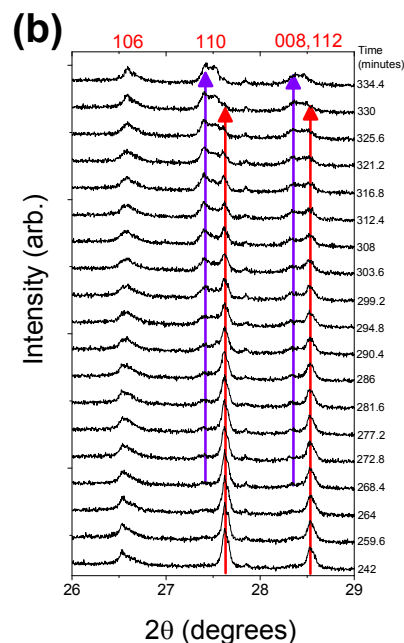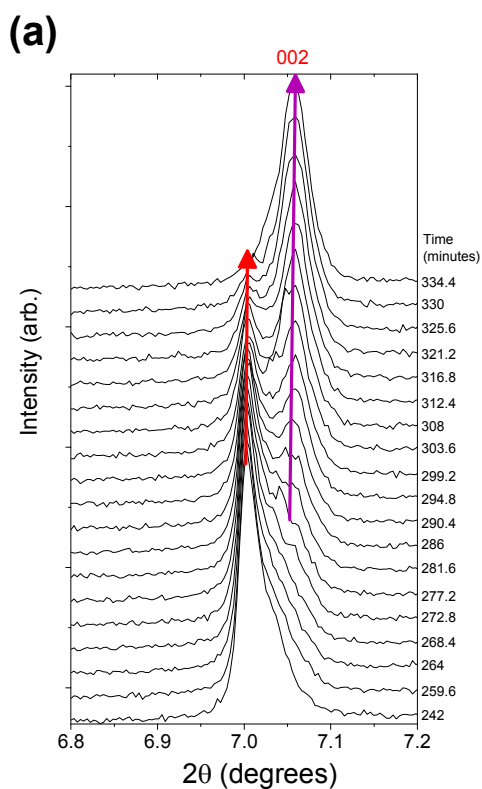
Figure 7. Snapshots via a stacked plot of the *in situ* data of the (a) 002 and (b) 106, 110, and 008, 112 reflections with time shown on the right hand side of each graph. The red arrows indicate the disappearance of reflections from initial phase (phase 1) and the purple reflections are the new reflections which show subtle changes in 2θ-value during the same region.

Detailed structural evolution during battery function:

For the sequential refinements 4 sections were defined. The first section until the two-phase reaction begins (half-filled symbols in Figure 8) corresponding to charge, discharge and part of the subsequent charge, the second section is the two-phase region (spheres in Figure 8), the third section leading up to the original $Na_{0.67}Mn_{0.8}Mg_{0.2}O_2$ composition on the 2nd charge (open symbols in Figure 8) and the last section is the reminder of charge (closed symbols in Figure 8).

During 1st charge *a* contracts while *c* expands until near the charged state where both *a* and *c* begin to stabilise around *a* = 2.8563(1) and *c* = 11.2528(3) Å. During the fast discharge *a* expands while *c* contracts and then stabilises with *a* ~ 2.87 and *c* ~ 11.18 Å and minimal change is observed during the initial stages of 2nd charge. This leads to the two-phase region (discussed below). At the end of the two-phase region *a* and *c* are at their highest and lowest values respectively, higher and lower than the original cathode and after discharging. Here *a* is 2.8879(1) and *c* is 11.1233(2) Å and the potential is 2.36 V. From this point on *a* contracts while *c* expands during the reminder of charge. Notably the contraction of *a* appears to be slightly more linear than the expansion of *c* as highlighted by the straight lines in Figure 8. This maybe intricately tied to the evolution of the sodium atomic parameters. The original composition of the cathode returns close to the open circuit potential (OCP) at 2.72 V (compared below). Interestingly, the charged cathode on 2nd charge resembles the charged electrode on 1st charge remarkably well suggesting robust and repeatable structural transitions during these processes.

On charge the Na content drops from 0.64(1) at OCP to 0.50(1) near the 1st charged state, corresponding to a change in Na content of the order of ~ 0.15. The electrochemically derived capacity for charge was 30 mAh g^{-1} which corresponds to a slightly lower change in Na content of ~0.14 Na. However, taking into account surface reactions and noting that the refinement was a constrained refinement the values give a good indication of the evolution. Interestingly the first 60 minutes of charge at 12 mA/g from OCP results in most of the sodium extraction occurring from the Na(2) site, which is then 'transferred' to the Na(1) site for the reminder of charge as indicated by the arrow in Figure 8. On the fast discharge, the sodium insertion occurs solely on the Na(1) site and the Na(2) occupancy remains the same. This suggests, sodium extraction occurs first from the Na(2) followed by the Na(1) site, while insertion occurs first to the Na(1) site. This shows that the Na(1) site has Na extracted from and inserted into near the charged state. However, sodium does not re-insert or transfer to the Na(2) site on charge. Even on subsequent charge the Na(2) site remains fairly constant. Thus Na(1) appears to carry the charge in this region (near 1st charged state, discharge, initial 2nd charge). The inability to extract more sodium from the Na(2) site during the initial part of the 2nd charge may be the reason that the two-phase region is observed. The two-phase region acts to re-distribute Na between the two crystallographic sites. This is evidenced after the two-phase region, where the Na occupancy is larger on the Na(2) site and smaller on the Na(1) compared to the beginning of the two-phase region. It appears that there is a need for Na re-distribution that instigates the two-phase region.
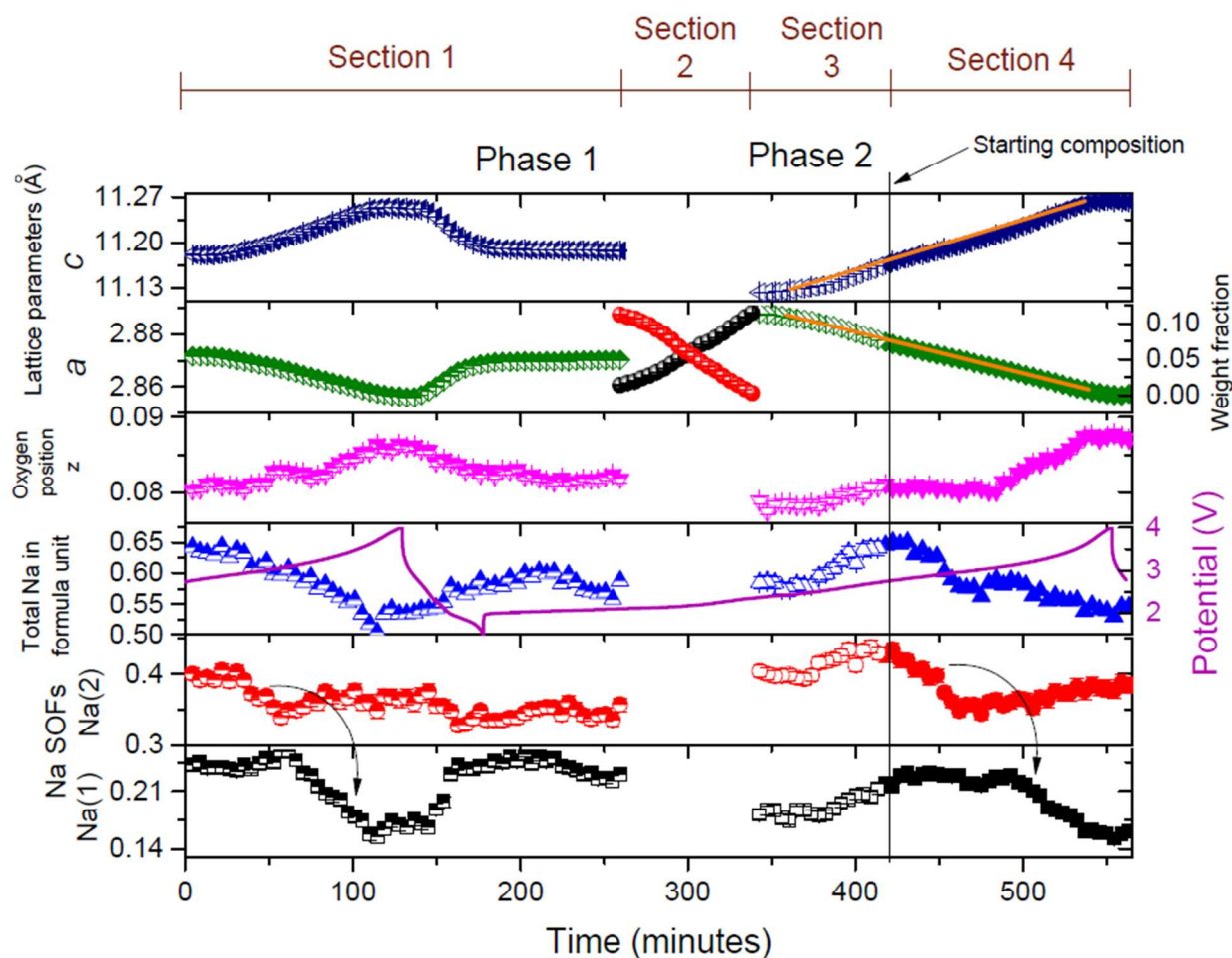
Figure 8. The evolution of the lattice parameters *a* and *c* in olive diamonds and blue triangles respectively, the phase fractions of the initial or 1st phase and the 2nd phase in red and black balls respectively, the oxygen positional parameters in magenta triangles, the total sodium content in the formula unit in blue triangles, the Na SOFs of the Na(1) and Na(2) sites in black squares and red circles respectively and the potential profile in purple. Half-filled symbols represent section 1 which encompasses the charge from OCP, discharge and initial 2nd charge process. The two phase region shown by only the black and red balls are considered as section 2. The section following the two-phase section as section 3 where the 2nd phase evolves in a rather anomalous fashion with respect to the sodium parameters and this section features open symbols. The final section, section 4 features filled symbols and begins from the composition and voltage that is equivalent to the OCP composition and voltage, as indicated by the straight line.

In the two-phase region (section 2) the 1st phase and a 2nd phase with slightly different lattice parameters and sodium content are active. The a, *c* lattice parameter and volume are 2.8879(1), 11.1233(1) Å and 80.343(3) Å^3 respectively at the end of the two-phase region (2nd phase) and at the beginning they are 2.8702(1), 11.1869(2) Å and 79.814(3) Å^3 (1st phase).

Thus the *a* lattice parameter expands, while *c* shrinks and the overall volume increases. The 2nd phase appears to be an expanded version of the initial 1st phase. Table 4 shows the major differences between the phases.

The one factor that appears at odds with the charge/discharge profile is the 3rd section which is shown by the open symbols in Figure 8, following the two-phase region. Here, the sodium content on both sites and overall increases and this occurs during charge where sodium extraction should be occurring. The speculative explanation for this behaviour can be that the presence of surface Na layers (following the two-phase region) allow for sodium extraction giving rise to the change in potential and charge process. While a small proportion of the surface Na equilibrates and locates onto the sites within the structure, increasing the bulk Na content. The *c* lattice parameter appears to be slightly non-linear in this region which may provide further insight for future work. Further work is required to rationalise the behaviour in this region of the charge process. In any case, following the $Na_{0.67}Mn_{0.8}Mg_{0.2}O_2$ composition on the 2nd charge (section 4), the behaviour observed from OCP to 1st charge (section 1) is essentially reproduced.

Table 4. Refined crystallographic parameters for $Na_{0.582(11)}Mn_{0.8}Mg_{0.2}O_2$ before the onset of the two-phase region and $Na_{0.578(11)}Mn_{0.8}Mg_{0.2}O_2$ (bold) after the two-phase region.

Atom	*Wyckoff*	*x*	*y*	*z*	SOF	Isotropic ADP $(\times 100)/Å^2$
Na(1)	2	0	0	0.25	0.228(7) **0.179(6)**	1.08[*] **0.53[*]**
Na(2)	2	1/3	2/3	0.75	0.354(9) **0.399(9)**	6.00[*,^] **6.99[*,^]**
Mn(1)	2	0	0	0	0.8	0.34[*,#] **0.13[*,#]**
Mg(1)	2	0	0	0	0.2	0.34[*,#] **0.13[*,#]**
O(1)	4	1/3	2/3	0.0816(5) **0.0786(5)**	1	1.40[*] **1.36[*]**

[*]Refined alternatively to SOFs and refined and fixed. ^ can be modelled anisotropically. # Constrained to be equal. Prior to two-phase region 34 refinement parameters, χ^2= 1.65, R_p = 2.59 %, wRp = 3.83 %, *a* = 2.8702(1), *c* = 11.1869(2) Å. After the two-phase region 34 refinement parameters, χ^2= 1.44, R_p = 2.43 %, wRp = 3.34 %, *a* = 2.8880(1), *c* = 11.1234(2) Å.

Comparing the initial phase in the coin cell at the open circuit potential (OCP) at 2.72 V and the structure in the subsequent charge at 2.72 V, there are minimal differences in the structure. Table 5 shows the atomic parameters for the structure at 2.72 V. The differences are minute, *a* OCP is 2.8717(1) compared to 2.8771(1) Å at the next 2.72 V on charge, *c* OCP is 11.1812(2) compared to 11.1672(2) Å, and volume OCP is 79.854(3) compared to 80.055(3) Å³. The similarities in the structure show its ability to reversibly insert/extract Na, with only a small expansion of *a* contraction of *c* noted at the same states of charge.

Table 5. Refined crystallographic parameters for $Na_{0.64(1)}Mn_{0.8}Mg_{0.2}O_2$ at 2.72 V on 2nd charge.

Atom	*Wyckoff*	*X*	*y*	*z*	SOF	Isotropic ADP $(\times 100)/Å^2$
Na(1)	2	0	0	0.25	0.218(6)	**0.53[*]**
Na(2)	2	1/3	2/3	0.75	0.421(10)	**6.99[*,^]**
Mn(1)	2	0	0	0	0.8	**0.13[*,#]**
Mg(1)	2	0	0	0	0.2	**0.13[*,#]**
O(1)	4	1/3	2/3	0.0808(5)	1	**1.36[*]**

[*]Refined alternatively to SOFs and refined and fixed. ^ can be modelled anisotropically. # Constrained to be equal. Space group = $P6_3/mmc$, 34 refinement parameters, χ^2= 1.69, R_p = 2.57 %, wRp = 3.90 %, *a* = 2.8771(1), *c* = 11.1672(2) Å.

Discussion

Overall, the structural transitions are reversible and at the 12 mA/g charge and 100 mA/g discharge there are single and two phase reactions occurring but the P2-type structure is preserved. At this rate there is no evidence of the *Cmcm* phase on discharge *via* these *in situ* measurements. From the *ex situ* measurements, it was concluded that the lack of the *Cmcm* phase and preservation of the P2 structure leads to a lower capacities of the $Na_{2/3}Mn_{0.8}Mg_{0.2}O_2$ cathode at 12 / 200 mA/g and 12 / 400 mA/g compared to 12 / 100 mA/g rates. However, the lack of the *Cmcm* phase during *in situ* experiments suggests a minute quantity may form under continuous operation at 12 / 100 mA/g.

A concern with the coin cell used in this work, containing circular Kapton-tape covered holes to allow X-ray transmission, as compared to cells with Be windows or the AMPIX cell[30] is the potential for a "lag effect" of the electrochemical reaction in the region of the hole. In other words, the XRD pattern is taken of a region that maybe behind the true electrochemistry of the cell. In order to test this, *in situ* cells with the $Na_{0.67}Mn_{0.8}Mg_{0.2}O_2$ electrode were tested offline under two conditions at the 200 mA/g discharge rate. The first cell was discharged to 1.5 V, allowed to rest before another discharge to 1.5 V was applied and this process was repeated 5 times. The second cell was just discharged to 1.5 V. Both cells were immediately extracted (~15 minutes, *via* a quick transfer to the glovebox). XRD data were collected using two slits that control the dimension of the incoming X-ray beam on the sample. The first dataset was collected with an incoming slit of 2 x ≤ 0.5 (vertical) mm dimension which was centered on the central part of the electrode and the second dataset with a slit of 4 x ≤ 0.5 (vertical) mm. The patterns clearly show the presence of a two phase electrode (see supporting information Figure S3). For the 100 mA/g discharge rate electrode using this slit configuration a similar two-phase electrode is observed but with a slightly different phase composition (see Figure S4). The two phase electrode at the 100 and 200 mA/g discharge rate in combination with the *in situ* synchrotron XRD data at the 100 mA/g discharge rate suggest that the process of electrode extraction allows the electrode to relax to a state that is not that kinetic state but rather closer to the thermodynamically stable state with two-phases present. Only slight variations in peak intensity are found between the 2 and 4 mm slits indicating that the regions with the Kapton window does not "lag" significantly behind the majority of the electrode as expected for these materials. In addition, there are significant differ-

ences in phase composition (see supporting information Figure S3 and S4) between the electrodes that are straight discharged at 100 mA/g and 200 mA/g, and sequentially discharged-rest-discharged, further illustrating the role electrode relaxation has on the processes under investigation. It is important to note that *in situ* (*operando*) processes can detail kinetic information, while extracting electrodes for *ex situ* studies can result in the convolution of the actual electrode state and any relaxation mechanisms that occur[31].

At 12 mA/g discharge the material delivers around 150 mAh/g[9] and the *Cmcm* phase is formed at the discharged state. As the discharge current rate is increased, there is an observed capacity loss, as there is less capacity that is extracted from the electrode, thus less of the *Cmcm* phase is formed at the discharged state. In other words, more of the *Cmcm* phase is formed at the 12 mA/g than the 100 mA/g discharge rate. The loss of capacity is a commonly seen occurrence as current rate is increased[32]. Coupling this behavior with the *in situ* XRD data, which shows that the *Cmcm* phase is not formed at the 100 mA/g discharge rate under continuous operation in contrast to *Cmcm* formation in *ex situ* studies suggests reaction kinetics plays a critical role.

The question of kinetics near the discharged state remains a complex problem. The rate limiting process and the process that limits capacity can be: the nucleation and growth of the *Cmcm* or P2 phase in all the particles (one particle can be P2 while another in *Cmcm*) or within particles (e.g. core/shell of P2 and *Cmcm* phases)[33-35]; related to the diffusion of sodium in the P2 and *Cmcm* phases; lattice avoidance of the two phase mechanism[29-30]; electronic/ionic conductivity of the electrode particle surface and bulk; or combinations of these processes to name a few options. Further work is required to rationalise such intricacies.

If one considers the percentage of the *Cmcm* phase formed for the 100 mA/g, 200 mA/g and 400 mA/g discharge, there is a distinct reduction in quantity from ~ 78, 25 to less than 0.2 % respectively (see Table 2 for ratios) *via ex situ* data after 100 cycles. Factoring in the *in situ* data collected at a discharge rate of 100 mA/g with no evidence of the *Cmcm* phase, the most likely cause of the formation of the *Cmcm* phase at 100 and 200 mA/g is electrode relaxation and extraction. Based on this information, and the recorded capacity at 400 mA/g, it is reasonable to suggest that the electrode does not reach the state of charge required where the *Cmcm* phase can form and thus any electrode relaxation will result in the P2 phase being maintained at 400 mA/g.

Sodium extraction (and insertion) often results in phase transitions, some dramatic and some minimal, during battery charge (or discharge) in this family of layered compounds[13,17,36]. Typically, as the current rate is increased, the amount of sodium extracted (or inserted) decreases which corresponds to a lower measured energy density or capacity. During the charge process in $Na_{0.67}Mn_{0.8}Mg_{0.2}O_2$, there is a phase transition between two P2-type or hexagonal $P6_3/mmc$ phases and this results in minimal structural change. In contrast, the hexagonal $P6_3/mmc$ to orthorhombic *Cmcm* phase transition near the discharged state appears to be one of the most significant factors that influence capacity and the largest structural change exhibited by this electrode. These phases are often referred to as P2 and P'2, respectively and are also observed in other P2-type electrodes[13,36]. The details of the hexagonal $P6_3/mmc$ to orthorhombic *Cmcm* transition are elegant-

ly detailed in ref.[36] which shows that with increasing Jahn-Teller active Mn^{3+} a cooperative distortion occurs that promotes this phase transition. Similar to the work on the $Na_xFe_{0.5}Mn_{0.5}O_2$, there appears to be a two-phase mixture at the end of discharge *via ex situ* measurements[36], but our *in situ* and *ex situ* findings suggest that this is a rate dependent reaction which does not occur at higher applied discharge rates.

Conclusions

The discharge current rate can influence the electrochemical performance of electrodes and there is a structural reason attributable to this in the case of $Na_{0.67}Mn_{0.8}Mg_{0.2}O_2$ electrodes. The transition of the $P6_3/mmc$ to the *Cmcm* phase at the discharged state is in part responsible for the marginally superior electrochemical performance with a discharge rate of 100 mA/g compared to the discharge rates of 200 and 400 mA/g. Although in an *ex situ* experiment, the *Cmcm* phase is clearly present at the discharged state with a 100 mA/g discharge rate, under real cell conditions (e.g. non-equilibrium) the *Cmcm* phase is not formed at the discharged state. The *Cmcm* phase does begin to form if the electrode is extracted from the cell, suggesting that the 100 mA/g discharge rate inhibits the formation of the *Cmcm* phase under continuous cycling conditions. From a chemical point-of-view, the nucleation and growth of the *Cmcm* phase and subsequent removal enhances the capacity of the electrochemical process, e.g. allowing sodium to be inserted into the *Cmcm* phase and thus increasing capacity. At higher discharge rates of 400 mA/g there is insufficient utilisation of the electrode which can lead to lower capacities compared to the 100 and 200 mA/g discharge rate. Therefore, the two-phase phase electrode or moving towards a two-phase electrode at the discharged state appears to be a prerequisite for better cycling performance. The current-rate dependent performance is intricately linked to the structure of electrodes and characterising this link will allow researchers and industry to maximise the performance of electrode materials. A synergy is required between the electronic controls of current rate during operation and the expected structural-electrochemical performance parameters.

ASSOCIATED CONTENT

Supporting information
Galvanostatic cycling, capacity versus cycle number of electrodes with different loadings, *ex situ* XRD analysis of electrodes extracted from coin cells with holes covered by Kapton tape.

AUTHOR INFORMATION

Corresponding Author

* N. Sharma, +61 2 93854714, Neeraj.sharma@unsw.edu.au
* T. Rojo, +34 945297108, trojo@cicenergigune.com

Author Contributions

The manuscript was written through contributions of all authors. All authors have given approval to the final version of the manuscript.

ACKNOWLEDGMENT

support through the research fellowship scheme. Part of this research was undertaken on the Powder Diffraction beamline at the Australian Synchrotron, Victoria, Australia. CIC Energigune work was financially supported by Ministerio de Economía y Competitividad (Proyecto I+D. Retos 2013), reference number: ENE 2013-44330-R and FPDI-2013-17329, and the Gobierno Vasco/EuskoJaurlaritza (Etortek CICEnergigune 10, SAIOTEK-12 ENERGIBA and IT570-13). PGB is indebted to the EPSRC, including the SUPERGEN programme, for financial support

REFERENCES

(1) Whittingham, M. S. Chemistry of intercalation compounds: Metal guests in chalcogenide hosts. *Prog. Solid State Chem.* **1978**, *12*, 41.

(2) Palomares, V.; Serras, P.; Villaluenga, I.; Hueso, K. B.; Carretero-Gonzalez, J.; Rojo, T. Na-ion batteries, recent advances and present challenges to become low cost energy storage systems. *Energy Environ. Sci.* **2012**, *5*, 5884.

(3) Palomares, V.; Casas-Cabanas, M.; Castillo-Martinez, E.; Han, M. H.; Rojo, T. Update on Na-based battery materials. A growing research path. *Energy Environ. Sci.* **2013**, *6*, 2312.

(4) Han, M. H.; Gonzalo, E.; Singh, G.; Rojo, T. A comprehensive review of sodium layered oxides: powerful cathodes for Na-ion batteries. *Energy Environ. Sci.* **2015**, *8*, 81.

(5) Delmas, C.; Fouassier, C.; Hagenmuller, P. Structural classification and properties of the layered oxides. *Physica B* **1980**, *99B*, 81.

(6) Yabuuchi, N.; Kajiyama, M.; Iwatate, J.; Nishikawa, H.; Hitomi, S.; Okuyama, R.; Usui, R.; Yamada, Y.; Komaba, S. P2-type $Na_x[Fe_{1/2}Mn_{1/2}]O_2$ made from earth-abundant elements for rechargeable Na batteries. *Nat. Mater.* **2012**, *11*, 512.

(7) Paulsen, J. M.; Dahn, J. R. Studies of the layered manganese bronzes, $Na_{2/3}[Mn_{1-x}M_x]O_2$ with M = Co, Ni, Li, and $Li_{2/3}[Mn_{1-x}M_x]O_2$ prepared by ion-exchange. *Solid State Ionics* **1999**, *126*, 3.

(8) Parant, J.-P.; Olazcuaga , R.; Devalette, M.; Fouassier, C.; Hagenmuller, P. Sur Quelques Nouvelles Phases de Formule Na_xMnO_2 (x ≤ 1). *J. Solid State Chem.* **1971**, *3*, 1.

(9) Billaud, J.; Singh, G.; Robert Armstrong, A.; Gonzalo, E.; Roddatis, V.; Armand, M.; Rojo, T.; Bruce, P. G. $Na_{0.67}Mn_{1-x}Mg_xO_2$ (0≤x≤0.2): a high capacity cathode for sodium-ion batteries. *Energy Environ. Sci.* **2014**, *7*, 1387.

(10) Yabuuchi, N.; Hara, R.; Kubota, K.; Paulsen, J.; Kumakura, S.; Komaba, S. New electrode material for rechargeable sodium batteries: P2-type $Na_{2/3}[Mg_{0.28}Mn_{0.72}]O_2$ with anomalously high reversible capacity. *J. Mater. Chem. A* **2014**, *2*, 16851.

(11) Sathiya, M.; Ramesha, K.; Rousse, G.; Foix, D.; Gonbeau, D.; Prakash, A. S.; Doublet, M.-L.; Hemalatha, K.; Tarascon, J. M. High Performance $Li_2Ru_{1-y}Mn_yO_3$ (0.2≤y≤0.8) Cathode Materials for Rechargeable Lithium-Ion Batteries: Their Understanding. *Chem. Mater.* **2013**, *25*, 1121.

(12) Kim, D.; Kang, S.-H.; Slater, M.; Rood, S.; Vaughey, J. T.; Karan, N.; Balasubramanian, M.; Johnson, C. S. Enabling Sodium Batteries Using Lithium-Substituted Sodium Layered Transition Metal Oxide Cathodes *Adv. Energy Mater.* **2011**, *1*, 333.

(13) Yoshida, H.; Yabuuchi, N.; Komaba, S. $NaFe_{0.5}Co_{0.5}O_2$ as high energy and power positive electrode for Na-ion batteries. *Electrochem. Commun.* **2013**, *34*, 60.

(14) Coelho, A. A. Whole-profile structure solution from powder diffraction data using simulated annealing. *J. Appl. Cryst.* **2000**, *33*, 899.

(15) Brant, W. R.; Schmid, S.; Du, G.; Gu, Q.; Sharma, N. A simple electrochemical cell for in-situ fundamental structural analysis using synchrotron X-ray powder diffraction. *J. Power Sources* **2013**, *244*, 109.

(16) Gummow, R. J.; Sharma, N.; Feng, R.; Han, G.; He, Y. High Performance Composite Lithium-Rich Nickel Manganese Oxide Cathodes for Lithium-Ion Batteries. *J. Electrochem. Soc.* **2013**, *160*, A1856.

(17) Sharma, N.; Gonzalo, E.; Pramudita, J. C.; Han, M. H.; Brand, H. E. A.; Hart, J. N.; Pang, W. K.; Guo, Z.; Rojo, T. The unique structural evolution of the O3-phase $Na_{2/3}Fe_{2/3}Mn_{1/3}O_2$ during high

rate charge/discharge: A sodium-centred perspective. *Adv. Funct. Mater.* **2015**, *25*, 4994.

(18) Sharma, N.; Serras, P.; Palomares, V.; Brand, H. E. A.; Alonso, J.; Kubiak, P.; Fdez-Gubieda, M. L.; Rojo, T. The sodium distribution and reaction mechanisms of a $Na_3V_2O_2(PO_4)_2F$ electrode during use in a sodium-ion battery. *Chem. Mater.* **2014**, *26*, 3391.

(19) Serras, P.; Palomares, V.; Rojo, T.; Brand, H. E. A.; Sharma, N. Structural evolution of high energy density V^{3+}/V^{4+} mixed valent $Na_3V_2O_{2x}(PO_4)_2F_{3-2x}$ (x = 0.8) sodium vanadium fluorophosphate using in-situ synchrotron X-ray powder diffraction. *J. Mater. Chem. A* **2014**, *2*, 7766.

(20) Pramudita, J. C.; Schmid, S.; Godfrey, T.; Whittle, T.; Alam, M.; Hanley, T.; Brand, H. E. A.; Sharma, N. Sodium uptake in cell construction and subsequent in operando electrode behaviour of Prussian Blue Analogues, $Fe[Fe(CN)_6]1-x.yH_2O$ and $FeCo(CN)_6$. *Phys.Chem. Chem. Phys.* **2014**, *15*, 24178.

(21) Duffort, V.; Talaie, E.; Black, R.; Nazar, L. F. Uptake of CO_2 in Layered P2-$Na_{0.67}Mn_{0.5}Fe_{0.5}O_2$: Insertion of Carbonate Anions. *Chem. Mater.* **2015**, *27*, 2515.

(22) K. S. Wallwork; B. J. Kennedy; D. Wang The High Resolution Powder Diffraction Beamline for the Australian Synchrotron. *AIP Conference Proceedings* **2007**, 879.

(23) Larson, A. C.; Von Dreele, R. B.; Los Alamos National Laboratory Report LAUR 86-748: 1994.

(24) Toby, B. H. EXPGUI, a graphical user interface for GSAS. *J. Appl. Cryst.* **2001**, *34*, 210.

(25) Guignard, M.; Didier, C.; Darriet, J.; Bordet, P.; Elkaim, E.; Delmas, C. P2-Na_xVO_2 system as electrodes for batteries and electron-correlated materials. *Nature Mater.* **2013**, *12*, 74.

(26) Wang, Y.; Xiao, R.; Hu, Y.-S.; Avdeev, M.; Chen, L. P2-$Na_{0.6}[Cr_{0.6}Ti_{0.4}]O_2$ cation-disordered electrode for high-rate symmetric rechargeable sodium-ion batteries. *Nat. Commun.* **2015**, *6*, 6954.

(27) Takahashi, Y.; Kijima, N.; Tokiwa, K.; Watanabe, T.; Akimoto, J. Single-crystal synthesis, structure refinement and electrical properties of $Li_{0.5}CoO_2$. *J. Phys.: Condens. Matter* **2007**, *19*, 436202.

(28) Sharma, N.; Peterson, V. K.; Elcombe, M. M.; Avdeev, M.; Studer, A. J.; Blagojevic, N.; Yusoff, R.; Kamarulzaman, N. Structural changes in a commercial lithium ion battery during electrochemical cycling: An *in-situ* neutron diffraction study. *J. Power Sources* **2010**, *195*, 8258.

(29) Sharma, N.; Guo, X.; Du, G.; Guo, Z.; Wang, J.; Wang, Z.; Peterson, V. K. Direct Evidence of Concurrent Solid-Solution and Two-Phase Reactions and the Nonequilibrium Structural Evolution of $LiFePO_4$. *J. Am. Chem. Soc.* **2012**, *134*, 7867−7873.

(30) Borkiewicz, O. J.; Shyam, B.; Wiaderek, K. M.; Kurtz, C.; Chupas, P. J.; Chapman, K. W. The AMPIX electrochemical cell: a versatile apparatus for in situ X-ray scattering and spectroscopic measurements. *J. Appl. Cryst.* **2012**, *45*, 1261.

(31) Sharma, N.; Pang, W. K.; Guo, Z.; Peterson, V. K. In Situ Powder Diffraction Studies of Electrode Materials in Rechargeable Batteries. *ChemSusChem* **2015**, *8*, 2826.

(32) Sharma, N.; Peterson, V. K. Current dependency of lattice fluctuations and phase evolution of electrodes in lithium-ion batteries investigated by in situ neutron diffraction. *Electrochim. Acta* **2013**, *101*, 79.

(33) Orvananos, B.; Yu, H.-C.; Abdellahi, A.; Malik, R.; Grey, C. P.; Ceder, G.; Thornton, K. Kinetics of Nanoparticle Interactions in Battery Electrodes. *J. Electrochem. Soc.* **2015**, *162*, A965.

(34) Orvananos, B.; Malik, R.; Yu, H.-C.; Abdellahi, A.; Grey, C. P.; Ceder, G.; Thornton, K. Architecture Dependence on the Dynamics of Nano-$LiFePO_4$ Electrodes. *Electrochim. Acta* **2014**, *137*, 245.

(35) Bai, P.; Cogswell, D. A.; Bazant, M. Z. Suppression of phase separation in $LiFePO_4$ nanoparticles during battery discharge. *Nano Lett.* **2011**, *11*, 4890.

(36) Talaie, E.; Duffort, V.; Smith, H. L.; Fultz, B.; Nazar, L. F. Structure of the high voltage phase of layered P2-$Na_{2/3-z}[Mn_{1/2}Fe_{1/2}]O_2$ and the positive effect of Ni substitution on its stability†. *Energy Environ. Sci.* **2015**, *8*, 2512.

TOC: